

Single-Layer Subwavelength Femtosecond-Laser-Induced Confined Nanocrystallization in Multistack Dielectrics

Ruben Ricca[✉]* and Yves Bellouard^{ID}

Galatea Laboratory, Institute of Electrical and Micro Engineering, School of Engineering, Ecole Polytechnique Fédérale de Lausanne (EPFL), Rue de la Maladière 71b, Neuchâtel 2000, Swiss Confederation



(Received 24 December 2022; revised 20 February 2023; accepted 20 March 2023; published 12 April 2023)

We demonstrate extreme laser-induced modification confinement in a stack of dielectric layers, along the optical axis, without the use of tight focusing. Specifically, we show that an aperiodic distribution of layer thicknesses can effectively lead to the formation of subsurface laser-induced modifications, confined in a 100-nm single predefined layer only, without affecting the surrounding material. We argue that this confinement is correlated to a local electric field enhancement phenomenon occurring within a specific layer of the stack and we confirm this hypothesis with simulations. Concurrently, we demonstrate the presence of nanocrystallites in the laser-affected areas.

DOI: 10.1103/PhysRevApplied.19.044035

I. INTRODUCTION

Tightly focused femtosecond laser beams can trigger nonlinear absorption phenomena in the bulk of transparent materials [1]. The extreme peak power of femtosecond laser pulses can not only result in densification or self-organized structures, such as the nanogratings observed in fused silica, but also in local phase changes (amorphization or crystallization) in a variety of substrates, from plain materials [2,3] to thin films [4], including stacked multilayers [5–7].

In this work, we investigate a method to achieve subwavelength- and subsurface-confined laser-induced modifications along the optical propagation axis. The motivation is to create nanoscale crystallites and densified zones at predefined locations within the layer stack, while maintaining the integrity of the surface. Such structures are of interest for a variety of applications, including metlenses, anticounterfeiting marking and high-density data storage in durable materials. In addition, silicon and titanium oxide nanocrystals, reported here, have been investigated for application as single-photon emitters [8], electronics and photovoltaics [9], and biological applications [9,10].

In bulk substrates, spatial confinement of a Gaussian beam along the optical propagation axis can be achieved by tightly focusing it using high-numerical-aperture lenses

[11], as shown in Fig. 1(a). However, the extreme peak power of the highly confined beam also leads to extreme pressures (estimated to reach the terapascal level in certain cases [12]), making it difficult to induce stable material modifications without inducing cavitation. Overly tight focusing may also lead to undesired filamentation effects. Here, we propose a method based on stacked layers. Specifically, by exploiting the index dependence of the absorption threshold, we confine the energy, and therefore the modifications, *along* the optical propagation axis by creating a succession of i layers of differing absorption-energy threshold $E_{\text{tr},i}$.

II. CONFINED MODIFICATIONS IN MULTILAYERS

For a single pulse traveling through a layer stack, the succession of interfaces results in multiple Fresnel reflections, which reduce the intensity of the transmitted beam, through destructive interference between the reflected light and the rest of the incoming pulse. The reflection can be partial or total, depending on the wavelength of the laser, the choice of materials, and the thickness and number of layers. This multistack-layer construction principle is commonly used in highly efficient dielectric Bragg reflectors (DBRs) that reflect narrow spectral bands of light. Technically, the layered construction modulates the electric field of the propagating laser, with localized intensity minima and maxima, located within specific layers [see Fig. 1(b)]. Consequently, a nonlinear absorption threshold for a layer in the stack can be reached in specific locations [13]. In quarter-wave distributed Bragg gratings, nonlinear absorption is initiated within the high-index materials, due to their lower laser-modification threshold [14]. The

*ruben.ricca@alumni.epfl.ch

Published by the American Physical Society under the terms of the [Creative Commons Attribution 4.0 International license](#). Further distribution of this work must maintain attribution to the author(s) and the published article's title, journal citation, and DOI.

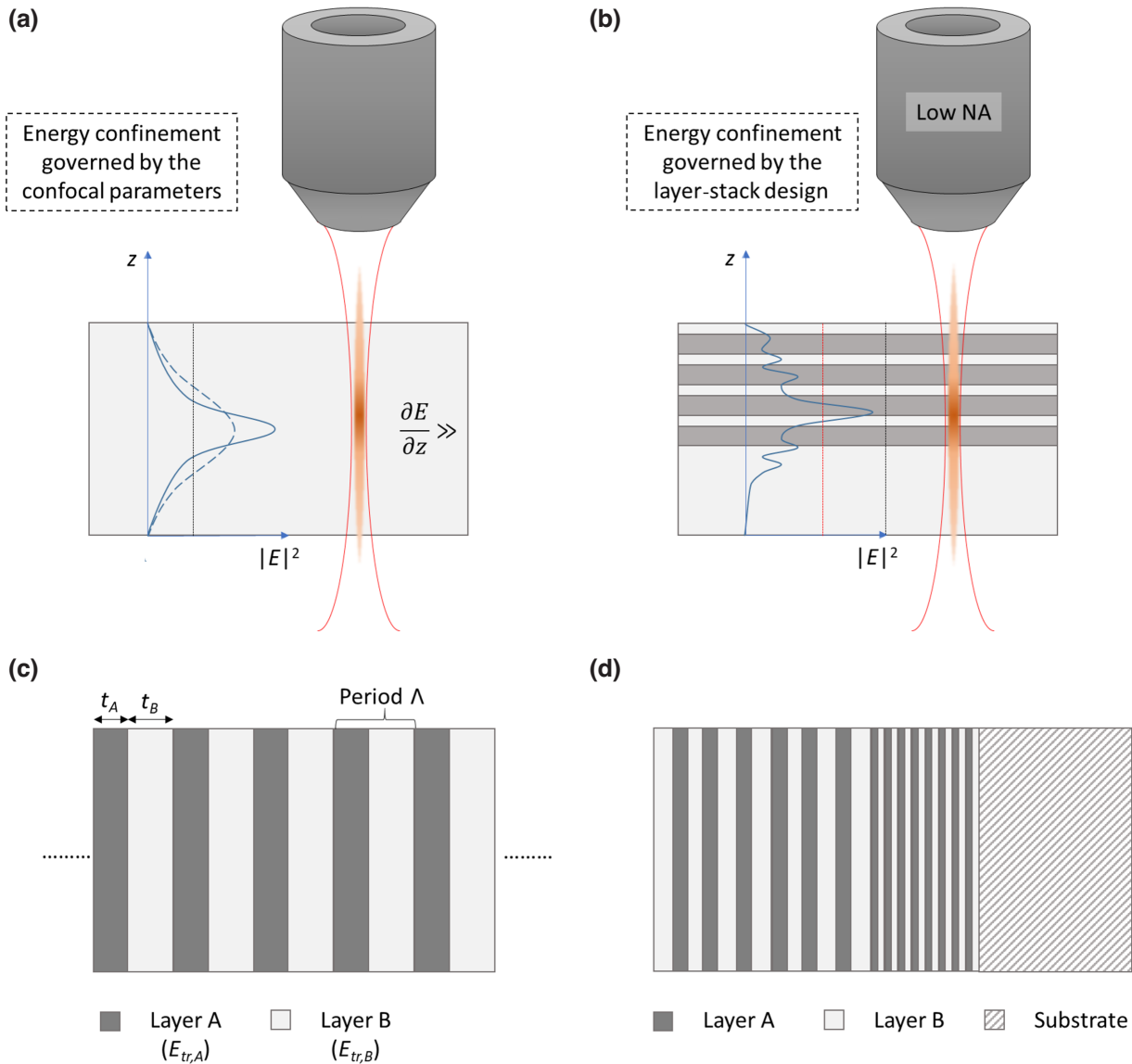


FIG. 1. (a) The electric-field-intensity ($|E|^2$) distribution along the beam-propagation direction, inside a homogeneous dielectric material. The continuous line corresponds to a high-numerical-aperture (NA) objective, while the dotted line corresponds to a lower NA value. The absorption threshold is represented as a black vertical line. Depending on the NA value, the affected area dimensions can vary. The higher the NA, the sharper is the intensity gradient and the smaller is the nonlinear affected zone. (b) Conversely, the concept of the modification process introduced in this paper. Consider a multilayer dielectric stack exposed to a femtosecond laser and designed to modulate the optical intensity profile as light propagates through it, due to the multiple reflections at the interfaces of the layers. The electric field modulation is schematically shown in blue: combined with the different absorption threshold of the constitutive materials, this modulation can enable a localized energy confinement along the propagation axis and, if it exceeds the absorption threshold, also laser-induced modifications limited to one or more specific layers, as opposed to being in a spherical volume (or an elliptical volume stretched along the optical axis), as observed when using a focusing technique based on a high-NA objective. In this illustration, the absorption threshold of the most sensitive material is represented as a red vertical line, while the threshold of the material most resistant to the laser radiation is shown in black. (c) A typical $\lambda/4$ DBR structure, with periodically repeating elements of thickness t_a and t_b , nonlinear absorption thresholds $E_{tr,A}$ and $E_{tr,B}$, and periodicity Λ . (d) An example of a design where the periodicity is disrupted, consisting of two sequential DBRs of different periodicities.

electric field can be further modulated by adapting the thickness and the composition of the layers [15], leading to a shift in the positions of the high-intensity peaks. This approach has been exploited as a means for reducing the

laser-induced damage threshold (LIDT) of optical components, as illustrated in Refs. [16–19].

To date, the studies on multistack layers have essentially focused on optimizing their structures to

prevent laser-induced damage. In a previous work [7], we have investigated how such a construction can also be used in the context of selectively introducing controlled laser modifications, such as localized crystallization, or as a means of inducing localized intermixing between layers.

In such cases, in addition to the multiple reflections at the layer interfaces, a feedback phenomenon arises from the pulse overlap when multiple pulses are directed at the same area. Indeed, each pulse induces structural changes in a pulse-to-pulse dynamically changing landscape. When the time separating two consecutive pulses is shorter than the heat relaxation time in the focal volume, the temperature gradually rises and a heat-dominated regime is observed, producing laser-affected zones that are significantly larger than the spot size. In the opposite case, the structure evolves stepwise, after each pulse, regardless of the time separating them, and in regions that can be smaller than the spot size. In both cases, each pulse interacts with a dynamically evolving landscape.

We formulate our research question as follows: how to induce a selective subsurface modification in a multilayer stack, limited to a single layer, so that the two adjacent layers remain unaffected.

III. MATERIALS AND METHODS

A. Multistack design

A commonly used multistack design for distributed Bragg reflectors is the quarter-wavelength ($\lambda/4$) design, which is typically used to create mirrors operating over specific spectral ranges. Here, a set of alternating bilayers of dielectric materials, where each individual layer has a thickness t_i inversely proportional to its refractive index n_i (following the equation $t_i = \lambda/4n_i$), repeats periodically a certain number of times [Fig. 1(c)]. The thicker the stack, the sharper is the central peak of reflectance. The layer-thickness arrangement also influences the location of high electric field intensity within the material, thus allowing for better control of the laser-induced damage threshold in dielectric mirrors.

According to the theory related to “dielectric Tamm waves,” described in Ref. [20,21], a localized field enhancement along the propagation axis in a specific location can be obtained if a rupture of periodicity is present in the multistack design. As an illustration, Kavokin *et al.* have demonstrated that two periodic layer-stack with different periodicities [see Fig. 1(d)] can effectively trigger a localized field enhancement near the boundary between the two stacks. Inspired by this work, we explore how these concepts can be used to trigger localized laser-induced modifications in selected locations within a multilayer.

In the sequel, we describe our experimental results, in an attempt to demonstrate experimentally the localized confinement. Specifically, we consider two sets of thin-film stacks, $\text{SiO}_2/\text{Si}_3\text{N}_4$ and $\text{SiO}_2/\text{TiO}_2$, respectively.

For the first case, $\text{SiO}_2/\text{Si}_3\text{N}_4$, we consider the case of an organized structure, albeit aperiodic. The second case, $\text{SiO}_2/\text{TiO}_2$, is a nearly random stacking of layers of different thicknesses and has been produced accidentally. Interestingly, this specimen resulting from serendipity, as we will show in what follows, offers a perfect illustration of the confinement effect in an aperiodic structure.

B. Sample preparation, processing, and analysis

The deposition of the $\text{SiO}_2/\text{TiO}_2$ sample is performed by magnetron sputtering on a Kenosistec system, while the deposition of the $\text{SiO}_2/\text{Si}_3\text{N}_4$ sample is done by PECVD, using an Oxford Plasmalab machine. The thicknesses of the individual layers are measured by analyzing the cross sections of the samples with a transmission electron microscope and can be found in Table SI of the Supplemental Material [22]. Note that the values of the refractive indexes are only indicative, as they do not result from direct measures but are taken from the literature [23–26]. Both depositions are done on 4-in. fused-silica wafers. A visual representation of the design of the layers can be seen in Fig. S1 in the Supplemental Material [22].

The light source is a femtosecond laser from Amplitude [Amplitude Systèmes (Pessac, France)], delivering pulses of 270 fs at 1030 nm. The pulse energy is controlled by tuning the acousto-optic modulator (AOM) efficiency at the laser level and by an automated half-wave plate and a polarized beam splitter in the optical path, while the pulse repetition rate can be modulated between 1 kHz and 3 MHz. In the present study, the repetition rate is chosen to be low enough so that there is no thermally cumulative effect. In such conditions, for a given exposure dose, the time interval between subsequent pulses does not play a role in how the material transforms. The beam is linearly polarized. The electric field orientation is controlled by rotating a half-wave plate placed between the beam splitter and the objective (20 \times , NA = 0.4). In this configuration, and considering the M^2 value of the laser, the Rayleigh length can be calculated as being 2.5 μm . The motion of the sample in the horizontal plane is enabled by a motorized stage (Micos/PI, Ultra-HR), with a displacement resolution of about 100 nm and repeatability around 200 nm. The scan speed needs to be varied according to the repetition rate and the desired laser net fluence (or exposure dose). The femtosecond-laser pulse train is then focused in the proximity of, and on the surface of, the multilayers (this distance depends on the confocal parameters) and the combination of the laser confocal parameters and the design of the layers results in the confinement of the modifications within a single layer, as illustrated in Fig. 1(b).

To quantify the energy involved in the process, the peak fluence F [Eq. (1)] and exposure dose E_d [Eq. (2)] [27] can

be defined, and calculated, as follows:

$$F = \frac{2E_p}{\pi w^2} (\text{J cm}^{-2}), \quad (1)$$

$$E_d = \frac{4E_p f}{\pi w s} (\text{J cm}^{-2}). \quad (2)$$

In these two equations, E_p corresponds to the pulse energy, w to the beam waist, f to the repetition rate of the pulses, and s to the scan speed of the stage. In all cases considered in this paper, s is kept at 1 mm/s, while $w = 0.9 \mu\text{m}$. The $\text{SiO}_2/\text{TiO}_2$ and $\text{SiO}_2/\text{Si}_3\text{N}_4$ samples are processed at repetition rates of 500 kHz and 1 MHz, respectively.

The processed samples are analyzed with scanning (SEM) and transmission (TEM) electron microscopy. The TEM lamellas are prepared with a focused ion beam (FIB)—specifically, using a Zeiss NVision 40 dual-beam SEM-FIB—by slicing cross sections of the multilayers and thinning them down to approximately 100 nm. The TEM observations are done on a Talos F200S from

ThermoFisher, operating at 200 kV, and include bright-field TEM (BF TEM), dark-field TEM (DF TEM), high-resolution TEM (HR TEM), selected-area electron diffraction (SAED), and energy-dispersive x-ray spectroscopy (EDS).

IV. EXPERIMENTAL RESULTS

Laser-induced modifications in the $\text{SiO}_2/\text{Si}_3\text{N}_4$ sample are highlighted by the BF-TEM image in Fig. 2(a). This area is exposed to the laser at a repetition rate of 1 MHz, a scan speed $s = 1 \text{ mm/s}$, and a pulse energy of 100 nJ, which in turn corresponds to a peak fluence of 7.86 J/cm^2 and an exposure dose of 14.15 kJ/cm^2 . The writing is done diagonally with respect to the surface, meaning that focal position is initially outside the sample and approaches the multilayers along the written line length, to finish below the multilayer level.

Following the exposure of this sample, the modifications are observed within a single layer of the high-index material, which in this case is Si_3N_4 , while the rest of the layers and the top surface of the sample are remarkably unaffected by the laser, so that the modifications reside

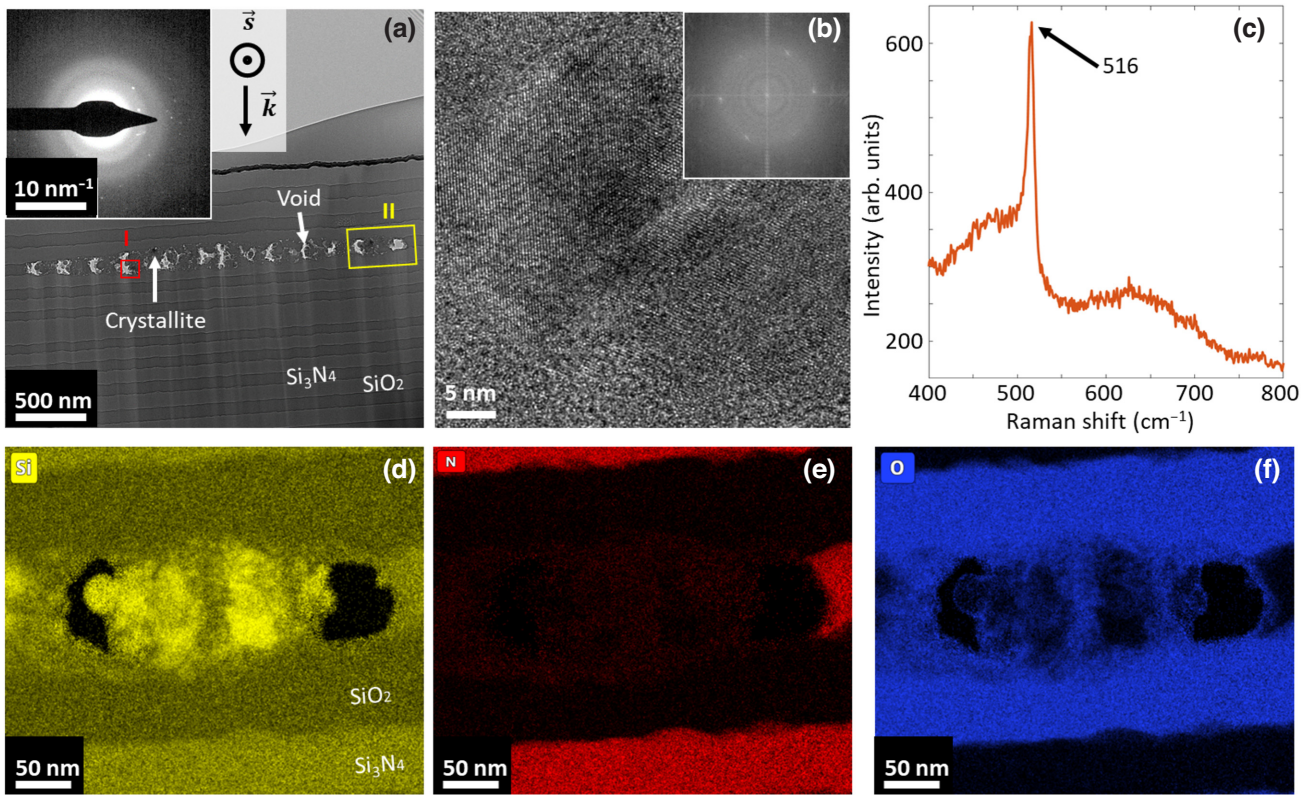


FIG. 2. (a)–(c) Confined modifications observed within the $\text{SiO}_2/\text{Si}_3\text{N}_4$ sample, with a BF TEM image of the affected area in (a) and the corresponding SAED pattern in the inset. Zone I (the red square) is further enlarged in (b), where a high-resolution image of the area is visible, showing the presence of oriented atomic planes corresponding to a crystalline material. The FFT of the HR image is shown in the inset. A Raman spectrum of the full laser-affected area is shown in (c), with a sharp peak at 516 cm^{-1} corresponding to crystalline diamond silicon. (d)–(f) The elemental distribution within the modified zone II (the yellow square) as measured with EDS, showing a sharp decrease in concentration of nitrogen, infiltration of oxygen, and clustering of silicon in the area.

exclusively within the stack itself. In BF-TEM mode, the contrast is created by electrons that are not diffracted by the material structure itself; as a result, highly diffracting crystalline structures appear darker. Therefore, the modified zone consists of alternating nanovoids (visible in white) and intermixed or crystallized regions visible as dark spots, alternating with an approximate periodicity of 200 nm. The presence of crystallites within the modified zone is confirmed by the SAED pattern, visible in the inset of Fig. 2(a), and by HR TEM [Fig. 2(b)], showing a globularlike polycrystal with regions of atomic planes oriented differently. This image is further processed to produce a fast-Fourier-transform (FFT) image [the inset in Fig. 2(b)] to obtain the frequency domain of the signal, resulting in discrete spots that can be used to retrieve the interplanar distance d_{hkl} for various planes of index hkl . The d_{hkl} values for different planar orientations are listed in Table I. The calculations are performed using Bragg's law with the hypothesis that the observed phase consists of diamond-structure silicon, which has a fcc structure with additional sites at positions $x, y, z = \frac{1}{8}, \frac{1}{8}, \frac{1}{8}$, resulting in a total of eight atoms per cell, and a lattice parameter $a = 0.543$ nm [29]. Table I shows that there is a good correlation between the experimental and theoretical data, with maximal deviations of 2.26, which are likely due to lattice distortions induced by residual stresses and volume mismatch between the crystallites and the surrounding amorphous matrix. Therefore, it can be stated that the laser-induced phase transition results in the creation of crystalline silicon clusters, as further evidenced by the Raman spectrum of the laser-affected zone in Fig. 2(c). The position of the sharp peak at 516 cm^{-1} , indicating the presence of crystallinity, is compatible with the spectrum of crystalline silicon [30]. The presence of silicon clusters is further illustrated by EDS elemental mapping,

TABLE I. A comparison of the measured and calculated interplanar distances for tetragonal rutile TiO_2 and fcc-diamond silicon, for a set of planar orientations, as well as the difference between these values (in percent). Values of both measured and calculated interplanar distances are expressed in angstroms.

Corresponding plane	Measured	Calculated	Difference
Rutile [28]			
(110)	3.357	3.247	+3.39
(101)	2.473	2.487	-0.56
(200)	2.259	2.296	-1.61
(210)	2.089	2.054	+1.70
(400)	1.141	1.148	-0.61
Diamond-Si [29]			
(111)	3.200	3.135	+2.07
(202)	1.900	1.919	-0.99
(212)	1.800	1.810	-0.55
(103)	1.700	1.717	-0.99
(113)	1.600	1.637	-2.26

showing a higher concentration of Si atoms within some locations of the modified zone [Fig. 2(d)], corresponding to the locations of the crystallites, while the behavior of nitrogen and oxygen [Figs. 2(e) and 2(f), respectively] is antithetical: while N atoms are getting depleted from that region, O atoms are infiltrating the modified area. This suggests a laser-induced modification phenomenon occurring in multiple steps, with bond breaking resulting from ionization at the beginning, followed by ionic migration and then recombination of a new crystalline phase.

Figure 3(a) shows the cross section of a laser-written line on the surface of the $\text{SiO}_2/\text{TiO}_2$ sample, imaged in BF-TEM mode, exposing the structure of the multilayers and of the laser-induced modifications. This particular region is irradiated with a repetition rate of 500 kHz, a scan speed of 1 mm/s, and a pulse energy of 234 nJ, resulting in a peak fluence of 18.39 J/cm^2 and an exposure dose of 16.55 kJ/cm^2 . A different repetition rate is chosen for the $\text{SiO}_2/\text{TiO}_2$ specimen to accommodate the different threshold repetition rate toward thermal accumulation for this specimen. The beam is focused $5 \pm 1\text{ }\mu\text{m}$ above the top surface. It should be noted that the actual exposure dose is reduced by a factor of $[(w/w)_0]^2$, as the irradiated area grows larger with the distance from the beam waist. As a result, at a distance of $5\text{ }\mu\text{m}$, the beam waist reaches a value of $2.01\text{ }\mu\text{m}$, resulting in an exposure dose of 3.32 kJ/cm^2 , or 5 times lower than at the focal spot. The lack of certainty about the positioning of the focal spot is caused by the tilt of the sample surface with respect to the optical axis, which in principle is measured and taken into account during the laser-processing step; however, given that the deposited energies lie around the nonlinear absorption threshold, micrometric displacements along the pulse propagation direction can still play a role in the triggering, or not, of nonlinear absorption.

As observed in the case of the $\text{SiO}_2/\text{Si}_3\text{N}_4$ sample, the modified zones are confined along the vertical direction within 100 nm, while the Rayleigh length in that case is $2.5\text{ }\mu\text{m}$, or 25 times larger. The presence of crystalline zones within the confined modifications is confirmed by Raman spectroscopy [Fig. 3(b)], with the measured curve showing a peak profile comparable to that of rutile [31], with deviations with respect to the literature data comprising between -1.1% and +2.8%. These deviations can be explained by the strain induced by the crystallites being surrounded by a continuous amorphous matrix and by periodic nanovoids, resulting in localized strain and therefore in slight peak shifts [32].

A larger view of the modified region is visible in Fig. 3(c), where it is possible to better distinguish the crystallites as darker spots within the TiO_2 layers. The presence of nanovoids (appearing in white), periodically spaced by around 150 nm, can also be noted, as there is an alternating pattern of crystalline regions and voids along the length of the layer. In this sense, the features of the modifications

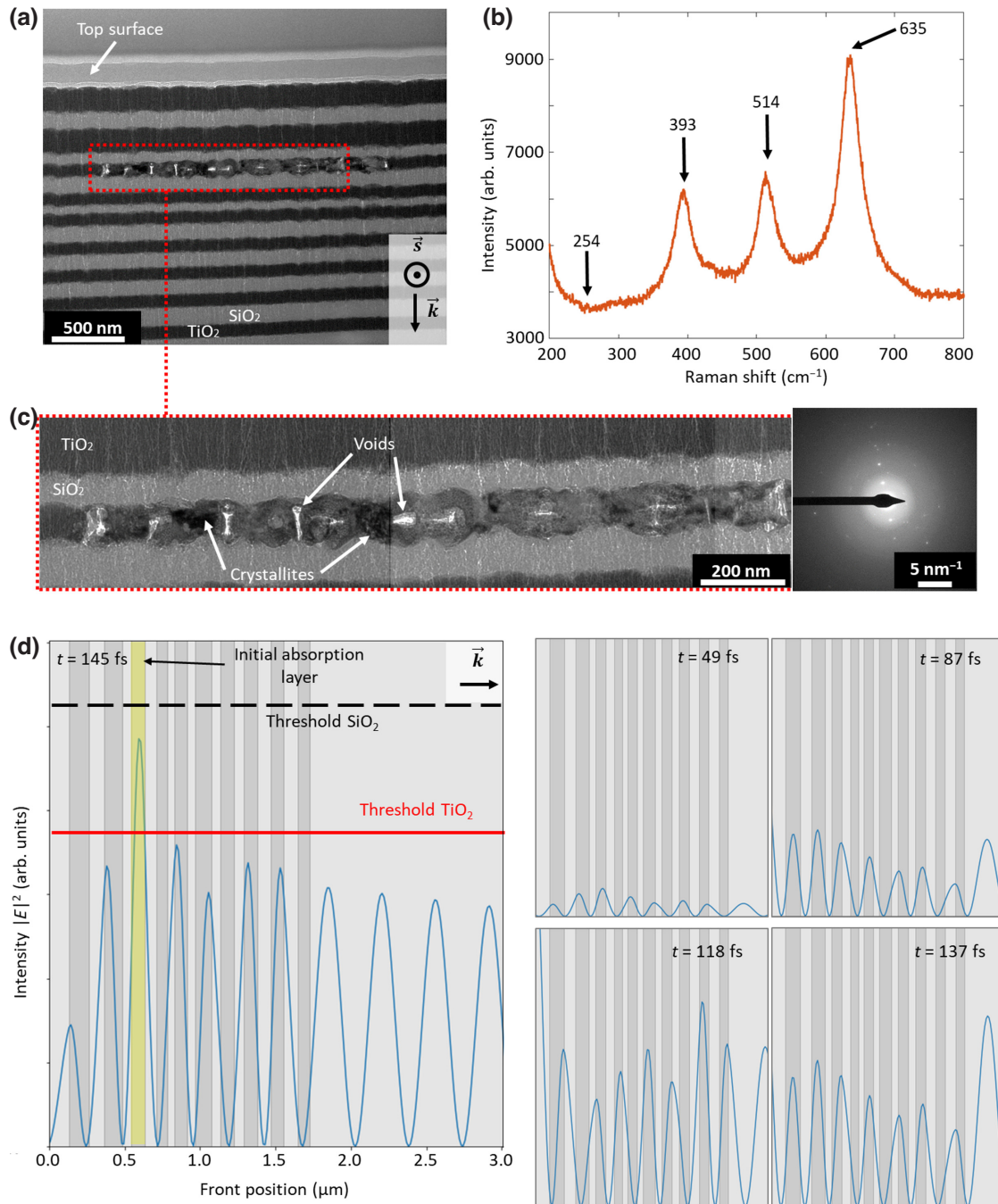


FIG. 3. (a) A BF-TEM image of a laser-modified $\text{SiO}_2/\text{TiO}_2$ multilayer stack and an illustration of the beam-propagation direction. The laser-induced modifications are confined to the third TiO_2 layer from the top. (b) The Raman curve measured at the exposed location, showing peak positions in agreement with a rutile- TiO_2 phase. (c) A BF-TEM image showing an enlargement of the modified zone, revealing the presence of both nanocrystallites and nanovoids, together with an inset showing a SAED pattern with clear spots attributed to electron diffraction from crystalline structures. (d) The simulation of the electric field profile inside the sample. The horizontal lines represent the hypothetical laser-induced modification thresholds for the materials of the layers. The high-index material (TiO_2) is shown in dark gray and the low-index material (SiO_2) is shown in light gray. On the right-hand side, the intensity evolution for previous times is also shown.

are similar to what has been observed in the $\text{SiO}_2/\text{Si}_3\text{N}_4$ sample (Fig. 2), albeit with smaller void regions. The inset shows a discrete SAED pattern, typical of a crystalline

material, which can be used to infer the interplanar distance for a set of orientations. Using Bragg's law, it is then possible to calculate the theoretical values of interplanar

distances for the same set hkl of Miller indices and to compare them to the experimental values. Since the Raman observations suggest the presence of a rutile phase, calculations are done according to the rutile crystal structure, which consists of a tetragonal phase with lattice parameters $a = 0.4593$ nm and $c = 0.2959$ nm [28]. Ti atoms occupy the corners, while O atoms occupy the sites at the positions $x, y, z = 0.3046, 0.3046, 0$. As is visible in Table I, there is good agreement between the measured and theoretical values of the interplanar distances, with minimal differences (between 0.56 and 3.39) that, similarly to what has been observed with Raman spectroscopy, can be attributed to residual stresses remaining after phase transition, lattice mismatch at the crystalline-amorphous interface, and observable inaccuracies during the measurement of the distances on the SAED image.

Finally, Fig. 3(d) shows the simulated movement of a femtosecond pulse through the $\text{SiO}_2/\text{TiO}_2$ sample, showing how the electric field is visibly enhanced in the third TiO_2 layer from the sample surface. The time stamp for this situation is $t = 145$ fs after the pulse reaches the multilayers surface, corresponding to the first instant at which the electric field intensity locally overcomes the threshold. To better visualize the evolution of the electric field intensity, snapshots of previous time stamps are enlarged and shown in the right-hand portion of the figure. As introduced in Sec. V, we argue that the intensity of the field at that location is above the nonlinear absorption threshold (as indicated by the horizontal red line), resulting in the laser-induced modifications reported in Figs. 3(a) and 3(c). Conversely, the pulse energy is still below the absorption threshold of the second material (SiO_2).

V. MODELING

To model the amplitude of modulation of the electric field inside the multilayer stack and to localize the sites of field enhancement, we perform electromagnetic field propagation simulations using a finite-difference time-domain (FDTD) method. In practice, we use the open-source code MEEP [33] and consider a nonchirped Gaussian source to simulate the pulse propagation. In a first approximation, we neglect the refractive-index dependence (Kerr effect) on the pulse intensity. The chromatic dispersions are also neglected. These approximations are reasonable in this case, since we are interested in the low-energy-pulse regime (just above the absorption threshold) and, hence, the nonlinear component of the refractive index remains small. The material properties are sourced from the MEEP database, even though in the case of TiO_2 the parameters are customized according to the literature [23]. The results obtained here show the pulse propagation in the form of the electric field intensity as function of the position along a cross section of the multilayers [Fig. 3(d)]. Another possibility for visualization is a cross section showing a

bidimensional illustration of the electric field. Figure 4 shows the beam-propagation simulation results, arranged top and bottom [Figs. 4(a) and 4(b)], for two different $\text{SiO}_2/\text{Si}_3\text{N}_4$ sample geometries, with a focal spot located 4 μm away from the surface of the layers and with the simulation taken at an instant $t = 90$ fs of the propagation through the multilayers. The left-hand part shows the structure of the layers: in Fig. 4(a), the multilayer structure consisting of a $\lambda/4$ DBR of eight bilayers, with individual layer thicknesses of $t_{\text{SiO}_2} = 120$ nm and $t_{\text{Si}_3\text{N}_4} = 90$ nm; and in Fig. 4(b), a symmetric arrangement around a central SiO_2 layer, from where the subsequent layer thicknesses increase gradually, as described in Table SI in the Supplemental Material [22]. The center of the figure illustrates interference between incoming and reflected waves for the two study cases. Finally, the right-hand part shows a filtered view of the interference patterns, highlighting the regions where the field intensity reaches an arbitrary threshold of 50 of the maximal intensity of the pulse. The effect of the design on the field enhancement is clearly visible: whereas in the case of the $\lambda/4$ design the electric field decays rapidly within the first few layers, in the second case the presence of the enhanced field is visible in specific locations within the stack of layers.

These simulations are restricted to the case of a single pulse propagating through the multilayers. A multipulse regime would imply consideration of a feedback mechanism, as each pulse gradually modifies the structure in which it propagates. In practice, the simulation should also incorporate evolving material properties after the passage of each pulse. Here, we limit ourselves to simulating the first step of the process, which is to localize the regions where nonlinear absorption will take place and to correlate these simulated zones of enhancement with the experimental observations.

With the help of these simulations, we argue that the field intensity reaches the modification threshold of the “weakest” material of the system, which is the high-index material, in a specific layer, where nonlinear absorption is initiated. The lack of modifications in the other material (the low-index material) and in the following layers of the “weak” material can be explained, respectively, by a highest modification threshold of the low-index material, which is not reached, and the absorption of the pulse energy in the first high-index layer where the threshold is reached, which is therefore “screening” the following layers.

VI. DISCUSSION

The correlation between FDTD simulations and experimental observations in the case of $\text{SiO}_2/\text{TiO}_2$ sample is appreciable, as the enhancement of the electric field in third layer of TiO_2 , starting from the surface, shown in Fig. 3(d), suggests that nonlinear absorption could have been initiated in this specific location, as is then demonstrated by

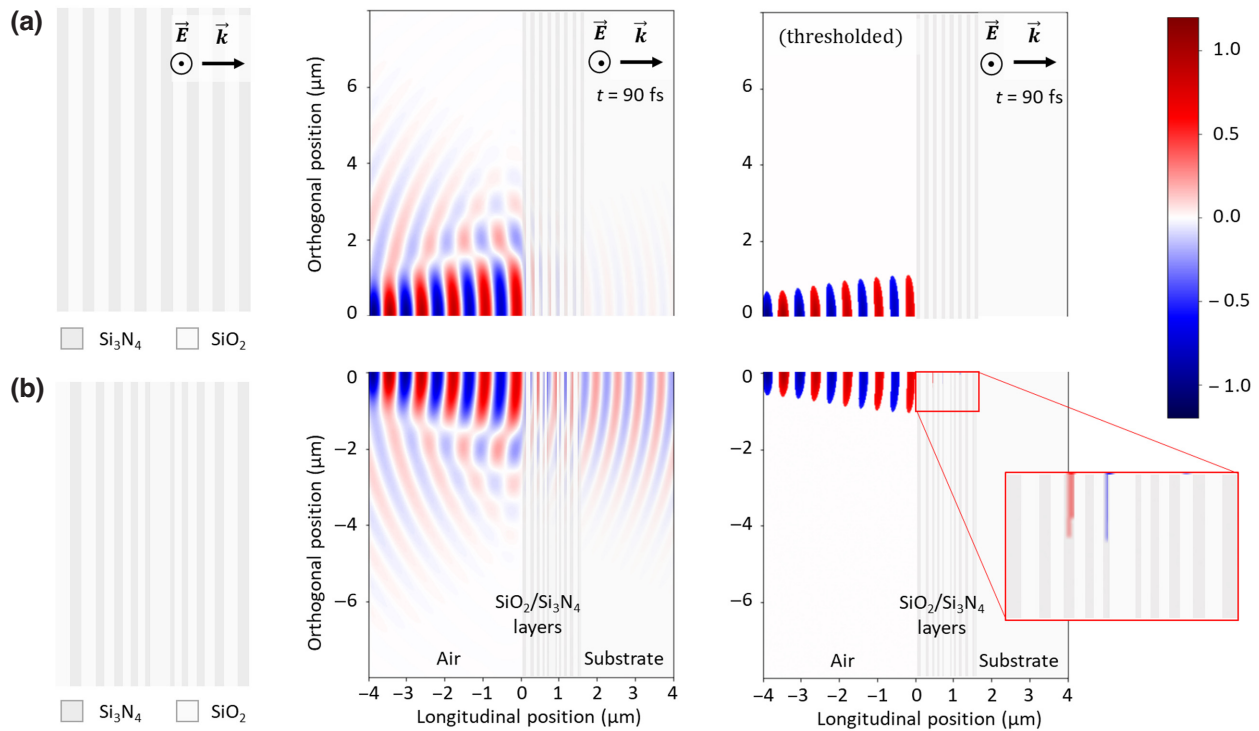


FIG. 4. An illustration of a Gaussian beam propagating in (a) a regular DBR and (b) through a $\text{SiO}_2/\text{Si}_3\text{N}_4$ layer with an aperiodic layers arrangement. As the k -vector axis defines an axis of symmetry for the electric field, only half of the field distribution is shown in both cases. The periodic design is a DBR corresponding to a $\lambda/4$ design ($t_{\text{SiO}_2} = 120 \text{ nm}$, $t_{\text{Si}_3\text{N}_4} = 90 \text{ nm}$) and the irregular one is described in the Supplemental Material [22] and is visible in Fig. 2. The exposure case simulated here is the one of a linearly polarized Gaussian beam propagating from left to right and corresponding to laser pulse lasting for a few hundred femtoseconds. The field intensity distribution is shown at a simulation time stamp of $t = 90 \text{ fs}$, defined from the time the pulse enters the material. The visualization plane is defined as perpendicular to the electric field orientation and along the k vector. The right-hand figure shows a filtered intensity map for a predefined absorption threshold. This particular time stamp corresponds to the case where a maximum electric field intensity is observed in one of the layers. The simulation predicts, first, a field-enhancement only in the case of the aperiodic design and, second, that the first layer along the propagation axis in which such enhancement occurs is the third one (see the inset), which effectively agrees with the experimental observations reported in Fig. 2.

the TEM images in Fig. 3. The proposed modification dynamic is as follows. The femtosecond beam is focused at a certain distance from the multilayer surface, such that the exposure dose is kept below the nonlinear absorption threshold of the materials of the layers. While traveling through the multilayer stack, the geometry and dielectric properties of the layers result in a local enhancement of the electric field of the pulse, specifically inside this specific TiO_2 layer, where nonlinear absorption is triggered and ionization occurs. Further absorption in the following layers is inhibited by the existence of a localized plasma that acts as a mirror within the initially modified layer (in which the damage threshold is decreased). The initiation of damage at the location of highest intensity has also been suggested in similar thin-film systems and for similar exposure conditions [34,35], although these studies have focused on the laser-induced damage threshold, and on the ejection of material, rather than on localized crystallization and controlled modification as we do here.

In the case of the Si_3N_4 sample, unfortunately, the focal spot accuracy along the optical axis compared to the size of the multistack layers does not allow for a precise correlation with the FDTD simulations. However, a confinement is obtained in the layers where higher electric field is expected and it manifests itself through the occurrence of nanocrystallites, as shown in Fig. 2, despite the short interaction time of the laser.

The crystallization dynamics of dielectric materials after exposure to femtosecond laser radiation are a source of debate, as the process itself is out of thermodynamic equilibrium. Laser-induced crystallization has been studied in semiconductor films, notably on amorphous silicon [36], where uniform and localized crystallization could be induced, and germanium [37], where the suggested crystallization mechanism is linked to the preferential absorption of IR radiation of Ge nanoclusters. Crystallization phenomena in semiconducting multilayers has also been studied in Ref. [38], where the crystallization of Ge is linked

to the destabilization of the lattice due to local increase in temperature and to the mismatch in thermal expansion coefficient between the two constituting materials. A previous study has linked the crystallization of TiO_2 to the effect of local lattice defects, which act as nucleation points after localized laser-induced heating [39]. Other studies have been performed on bulk glass substrates using a pulsed laser in the picosecond regime and have been linked to the thermal gradient [40], which is believed to induce a phase separation. Finally, Liu *et al.* [41] have also postulated a crystallization process mediated by local temperature gradients through thermal accumulation, in the femtosecond regime.

In this study, femtosecond lasers emitting 270-fs pulses applied on dielectric stacks are proven to be effective in promoting nucleation sites for crystallization, even though the crystallization dynamics remain elusive due to the actual lack of time-lapse observations.

In this case, and compared to these previous studies, there is no thermal process occurring beyond the focal volume, as evidenced in the *post mortem* observations. Furthermore, the repetition rate of the laser is chosen to be in a range where no thermally cumulative effect is observed. The energy is also chosen such that it is confined in a single layer only. In addition, the TEM observations along with the elemental distribution clearly show that adjacent layers are unaffected during the process, hence demonstrating that no thermal degradation is occurring and that the temperature in these layers remains lower than any critical temperature.

As expected, there is a difference in the crystallization dynamics between the two material systems, as laser exposure of the $\text{SiO}_2/\text{TiO}_2$ sample results in a TiO_2 crystalline polymorph, rutile, while exposure of the $\text{SiO}_2/\text{Si}_3\text{N}_4$ sample initiates a Si crystalline phase. Hence, in the TiO_2 case, the stoichiometry of the material is maintained, as the material likely undergoes a laser-induced ordering of its own microstructure. The local increase in temperature, as well as the compressive pressure applied by the surrounding layers, enables the overcoming of the energy barrier necessary for the phase transformation. The rutile phase is, generally, energetically more stable than other TiO_2 polymorphs [42,43], which would explain the preferred transformation of the nonordered material into this specific phase. Interestingly, previous reports suggest that anatase should be the preferred phase for nanoparticles of a diameter of the order of 10 nm, due to the lower surface energy of this phase compared to rutile [44]. It has also been shown that anatase might have a faster kinetic of crystallization and, therefore, might be favored at lower temperatures, at the early stage of classical phase-transition processes (e.g., in a furnace) [42]. Here, however, due to the nature of the laser-matter interaction, this is clearly not case, suggesting a more dramatic phase-transformation mechanism, from a “nano”-plasma phase to a crystalline one. As we do

post mortem analysis of the crystallized samples, we are unable to observe the crystallization process—which may involve multiple steps (e.g., amorphous to anatase, then to rutile)—as it happens, as the structures are produced by multipulse exposure.

A slight migration of Si atoms toward the modified TiO_2 layer is also observed (see Fig. S1 in the Supplemental Material [22]), even though it is mostly confined around the void regions and therefore might be explained by the diffusion of atoms toward available “empty” space. The concentration of oxygen does not appear to be altered between the affected and nonaffected zones, which is consistent with the fact that the stoichiometry of the new phase is unchanged with respect to the original amorphous material. In the second case, however, it is evident that the Si—N bonds in the affected Si_3N_4 layer are broken at a certain point of the process, as the Si atoms subsequently recombine into Si crystallites, while the N atoms diffuse outside of the affected zone, with a fraction of them probably escaping the material in gaseous form through micro- and macrocracks along the layers above. Such cracks are observed at some locations along the laser-written lines, indicating that some locations might exhibit greater damage across multiple layers and up to the surface. The diffusion of O inside the modified zone, which indicates that the surrounding SiO_2 layers are partially affected as well, is also of relevance.

VII. CONCLUSIONS AND OUTLOOK

By exploiting a phenomenon of localized field enhancement in one-dimensional aperiodic arrangements of layers, we demonstrate a method to achieve high spatial confinement of laser-induced modifications along the optical propagation axis, without the use of a tightly focused beam. Specifically, we show that laser-induced modifications in dielectric multilayers, notably localized crystallization, can be confined in one layer of a multilayer stack without affecting the surface of the material. The crystalline zones are much smaller than the wavelength of the processing laser and are up to 25 times smaller than the Rayleigh length for the focusing objective considered here.

The confinement is demonstrated in two different material systems, namely, $\text{SiO}_2/\text{Si}_3\text{N}_4$ and $\text{SiO}_2/\text{TiO}_2$ multilayer samples, with different layer-thickness arrangements, confirming that this phenomenon is essentially driven by the layer-thickness distribution and validating the field-enhancement phenomenon. The experimental observation of field confinement is confirmed and predicted using a FDTD propagation model. The method is generic and can be applied to a broad variety of layers and/or assemblies. Although not investigated here, but nevertheless commonly observed for bulk-nanograting formation (see, e.g., Ref. [45]), the polarization state of the beam may also

offer an additional parameter for controlling the formation and possibly the orientation of the crystallites. Finally, this controlled high-confinement capability in the bulk of layered materials opens up interesting opportunities in various fields, including high-density durable data storage, metalenses, and nanocrystals for quantum emitters.

The data underlying the results presented in this paper are not publicly available at this time but may be obtained from us upon reasonable request.

ACKNOWLEDGMENTS

We acknowledge the Swiss National Science Foundation [Schweizerische Nationalfonds zur Förderung der wissenschaftlichen Forschung (SNF)—Fonds national suisse de la recherche scientifique (FNS)] for enabling this research through Grant No. CRSII5_180232. R.R. would like to thank Dr. Simone Frasca for his contribution for the deposition of the samples and Dr. Antoine Delgoffe for the helpful insights on the functioning of MEEP.

Y.B. and R.R. designed the experiments. R.R. performed the FDTD simulations, deposited the SiO₂/Si₃N₄ multi-layers, performed the experiments, and characterized the samples. R.R. and Y.B. discussed the experimental results and wrote the paper. Both of us revised and discussed the paper before submission. Y.B. designed and supervised the project.

We have submitted a patent related to this research [46].

-
- [1] D. Du, X. Liu, G. Korn, J. Squier, and G. Mourou, Laser-induced breakdown by impact ionization in SiO₂ with pulse widths from 7 ns to 150 fs, *Appl. Phys. Lett.* **64**, 3071 (1994).
 - [2] B. Zhang, Z. Wang, D. Tan, X. Liu, B. Xu, L. Tong, P. Kazansky, and J. Qiu, Ultrafast laser inducing continuous periodic crystallization in the glass activated via laser-prepared crystallite-seeds, *Adv. Opt. Mater.* **9**, 2001962 (2021).
 - [3] C. Florian, D. Fischer, K. Freiberg, M. Duwe, M. Sahre, S. Schneider, A. Hertwig, J. Krüger, M. Rettenmayr, U. Beck, A. Undisz, and J. Bonse, Single femtosecond laser-pulse-induced superficial amorphization and re-crystallization of silicon, *Materials* **14**, 1651 (2021).
 - [4] V. Volodin, T. Korchagina, J. Koch, and B. Chichkov, Femtosecond laser induced formation of Si nanocrystals and amorphous Si clusters in silicon-rich nitride films, *Phys. E* **42**, 1820 (2010).
 - [5] N. Farid, A. Brunton, P. Rumsby, S. Monaghan, R. Duffy, P. Hurley, M. Wang, K. Choy, and G. O'Connor, Femtosecond laser-induced crystallization of amorphous silicon thin films under a thin molybdenum layer, *ACS Appl. Mater. Interfaces* **13**, 37797 (2021).
 - [6] A. Larin, E. Ageev, L. Dvoretckaia, A. Mozharov, I. Mukhin, and D. Zuev, Formation of luminescent structures in thin a-Si:H-Er films irradiated by femtosecond laser pulses, *JETP Lett.* **114**, 681 (2021).
 - [7] R. Ricca, V. Boureau, and Y. Bellouard, Ultrafast laser interaction with transparent multi-layer SiO₂/Si₃N₄ films, *J. Appl. Phys.* **130**, 243105 (2021).
 - [8] A. Senichev, Z. Martin, S. Peana, D. Sychev, X. Xu, A. Lagutchev, A. Boltasseva, and V. Shalaev, Room-temperature single-photon emitters in silicon nitride, *Sci. Adv.* **7**, eabj0627 (2021).
 - [9] L. Mangolini, Synthesis properties, and applications of silicon nanocrystals, *J. Vac. Sci. Technol. B* **31**, 020801 (2013).
 - [10] J. Molina-Reyes, A. Romero-Moran, H. Uribe-Vargas, B. Lopez-Ruiz, J. Sanchez-Salas, E. Ortega, A. Ponce, A. Morales-Sanchez, F. Lopez-Huerta, and C. Zuñiga-Islas, Study on the photocatalytic activity of titanium dioxide nanostructures: Nanoparticles, nanotubes and ultra-thin films, *Catal. Today* **341**, 2 (2020).
 - [11] E. Glezer and E. Mazur, Ultrafast-laser driven micro-explosions in transparent materials, *Appl. Phys. Lett.* **71**, 882 (1997).
 - [12] S. Juodkazis, K. Nishimura, S. Tanaka, H. Misawa, E. Gamaly, B. Luther-Davies, L. Hallo, P. Nicolai, and V. Tikhonchuk, Laser-Induced Microexplosion Confined in the Bulk of a Sapphire Crystal: Evidence of Multimegarab Pressures, *Phys. Rev. Lett.* **96**, 166101 (2006).
 - [13] I. Angelov, M. Von Pechmann, M. Trubetskoy, F. Krausz, and V. Pervak, Optical breakdown of multilayer thin-films induced by ultrashort pulses at MHz repetition rates, *Opt. Exp.* **21**, 31453 (2013).
 - [14] M. Mero, J. Liu, W. Rudolph, D. Ristau, and K. Starke, Scaling laws of femtosecond laser pulse induced breakdown in oxide films, *Phys. Rev. B* **71**, 115109 (2005).
 - [15] L. Gallais, X. Cheng, and Z. Wang, Influence of nodular defects on the laser damage resistance of optical coatings in the femtosecond regime, *Opt. Lett.* **39**, 1545 (2014).
 - [16] G. Abromavicius, R. Buzelis, R. Drazdys, A. Melninkaitis, and V. Sirutkaitis, in *Boulder Damage Symp. XXXIX* (SPIE, Boulder, CO, USA, 2007), p. 67200Y.
 - [17] M. Chorel, T. Lanterrier, E. Lavastre, N. Bonod, B. Bousquet, and J. Néauport, Robust optimization of the laser induced damage threshold of dielectric mirrors for high power lasers, *Opt. Exp.* **26**, 11764 (2018).
 - [18] F. Kong, S. Chen, S. Liu, Y. Jin, H. Guan, Y. Du, C. Wei, H. He, and K. Yi, in *Pacific Rim Laser Damage Symp.* (SPIE, Shanghai, China, 2011), p. 82060P.
 - [19] G. Long and Y. Zhang, in *Second Symposium on Novel Technology of X-Ray Imaging* (SPIE, Hefei, China, 2019), p. 65.
 - [20] A. Kavokin, I. Shelykh, and G. Malpuech, Lossless interface modes at the boundary between two periodic dielectric structures, *Phys. Rev. B* **72**, 233102 (2005).
 - [21] C. Schmidt, A. Palatnik, M. Sudzius, S. Meister, and K. Leo, Coupled topological interface states, *Phys. Rev. B* **103**, 085412 (2021).
 - [22] See the Supplemental Material at <http://link.aps.org/supplemental/10.1103/PhysRevApplied.19.044035> for sample specifications and additional results.
 - [23] J. DeVore, Refractive indices of rutile and sphalerite, *J. Opt. Soc. Am.* **41**, 416 (1951).
 - [24] I. Malitson, Interspecimen comparison of the refractive index of fused silica, *J. Opt. Soc. Am.* **55**, 1205 (1965).

- [25] T. Siefke, S. Kroker, K. Pfeiffer, O. Puffky, K. Dietrich, D. Franta, I. Ohlidal, A. Szeghalmi, E. Kley, and A. Tünnermann, Materials pushing the application limits of wire grid polarizers further into the deep ultraviolet spectral range, *Adv. Opt. Mater.* **4**, 1780 (2016).
- [26] K. Luke, Y. Okawachi, M. Lamont, A. Gaeta, and M. Lipson, Broadband mid-infrared frequency comb generation in a Si₃N₄ microresonator, *Opt. Lett.* **40**, 4823 (2015).
- [27] S. Rajesh and Y. Bellouard, Towards fast femtosecond laser micromachining of fused silica: The effect of deposited energy, *Opt. Exp.* **18**, 21490 (2010).
- [28] D. Kim, N. Enomoto, Z. Nakagawa, and K. Kawamura, Molecular dynamic simulation in titanium dioxide polymorphs: Rutile, brookite, and anatase, *J. Am. Ceram. Soc.* **79**, 1095 (1996).
- [29] J. Cannon, Behavior of the elements at high pressures, *J. Phys. Chem. Ref. Data* **3**, 781 (1974).
- [30] J. Parker, D. Feldman, and M. Ashkin, Raman scattering by silicon and germanium, *Phys. Rev.* **155**, 712 (1967).
- [31] R. Verma, J. Gangwar, and A. Srivastava, Multiphase TiO₂ nanostructures: A review of efficient synthesis growth mechanism, probing capabilities, and applications in bio-safety and health, *RSC Adv.* **7**, 44199 (2017).
- [32] Y. Kang, Y. Qiu, Z. Lei, and M. Hu, An application of Raman spectroscopy on the measurement of residual stress in porous silicon, *Opt. Lasers Eng.* **43**, 847 (2005).
- [33] A. Oskooi, D. Roundy, M. Ibanescu, P. Bermel, J. Joannopoulos, and S. Johnson, MEEP: A flexible free-software package for electromagnetic simulations by the FDTD method, *Comput. Phys. Commun.* **181**, 687 (2010).
- [34] K. Kumar, K. Lee, J. Li, J. Nogami, N. Kherani, and P. Herman, Quantized structuring of transparent films with femtosecond laser interference, *Light: Sci. Appl.* **3**, e157 (2014).
- [35] A. Kozlov, J. Lambropoulos, J. Oliver, B. Hoffman, and S. Demos, Mechanisms of picosecond laser-induced damage in common multilayer dielectric coatings, *Sci. Rep.* **9**, 607 (2019).
- [36] K. Bronnikov, A. Dostovalov, A. Cherepakhin, E. Mitsai, A. Nepomiaschiy, S. Kulinich, A. Zhizhchenko, and A. Kuchmizhak, Large-scale and localized laser crystallization of optically thick amorphous silicon films by near-IR femtosecond pulses, *Materials* **13**, 5296 (2020).
- [37] K. Astankova, A. Kozhukhov, G. Krivyakin, Y. Zhivodkov, D. Sheglov, and V. Volodin, Interaction of low-fluence femtosecond laser pulses with a composite layer containing Ge nanoclusters: A novel type of nanofoam formation, *J. Laser Appl.* **34**, 022002 (2022).
- [38] V. Volodin, Y. Cheng, A. Bulgakov, Y. Levy, J. Beránek, S. Nagisetty, M. Zukerstein, A. Popov, and N. Bulgakova, Single-shot selective femtosecond and picosecond infrared laser crystallization of an amorphous Ge/Si multilayer stack, *Opt. Laser Technol.* **161**, 109161 (2023).
- [39] S. Ahmed, V. Poole, J. Igo, Y. Gu, and M. McCluskey, Localized phase transition of TiO₂ thin films induced by sub-bandgap laser irradiation, *J. Vac. Sci. Technol., A* **39**, 053402 (2021).
- [40] B. Zhang, D. Tan, X. Liu, L. Tong, P. Kazansky, and J. Qiu, Self-organized periodic crystallization in unconventional glass created by an ultrafast laser for optical attenuation in the broadband near-infrared region, *Adv. Opt. Mater.* **7**, 1900593 (2019).
- [41] Y. Liu, B. Zhu, L. Wang, Y. Dai, H. Ma, G. Lakshminarayana, and J. Qiu, Femtosecond laser direct writing of TiO₂ crystalline patterns in glass, *Appl. Phys. B* **93**, 613 (2008).
- [42] D. Hanaor and C. Sorrell, Review of the anatase to rutile phase transformation, *J. Mat. Sci.* **46**, 855 (2011).
- [43] M. Ranade, A. Navrotsky, H. Zhang, J. Banfield, S. Elder, A. Zaban, P. Borse, S. Kulkarni, G. Doran, and H. Whitfield, Energetics of nanocrystalline TiO₂, *Proc. Natl. Acad. Sci.* **99**, 6476 (2002).
- [44] S. Smith, R. Stevens, S. Liu, G. Li, A. Navrotsky, J. Boero-Goates, and B. Woodfield, Heat capacities and thermodynamic functions of TiO₂ anatase and rutile: Analysis of phase stability, *Am. Mineral.* **94**, 236 (2009).
- [45] Y. Shimotsuma, P. Kazansky, J. Qiu, and K. Hirao, Self-Organized Nanogratings in Glass Irradiated by Ultrashort Light Pulses, *Phys. Rev. Lett.* **91**, 247405 (2003).
- [46] R. Ricca, Y. Bellouard, and M. Vetterli, Patent Application No. EP22170715.1 (2022).